The Influence of Microstructure and Strength on the Fracture Mode and Toughness of 7XXX Series Aluminum Alloys

GERARD M. LUDTKA and DAVID E. LAUGHLIN

The effects of microstructure and strength on the fracture toughness of ultra high strength aluminum alloys have been investigated. For this study three ultra high purity compositions were chosen and fabricated into 1.60 mm (0.063 inches) sheet in a T6 temper providing a range of yield strengths from 496 MPa (72 ksi) to 614 MPa (89 ksi). These alloys differ only in the volume fraction of the fine matrix strengthening precipitates (G.P. ordered + η'). Fracture toughness data were generated using Kahn-type tear tests, as well as R-curve and J_c analyses performed on data from 102 mm wide center cracked tension panel tests. Consistent with previous studies, it has been demonstrated that the toughness decreases as the yield strength is increased by increasing the solute content. Concomitant with this decrease in toughness, a transition in fracture mode was observed from predominantly transgranular dimpled rupture to predominantly intergranular dimpled rupture. Both quantitative fractography and X-ray microanalysis clearly demonstrate that fracture initiation for the two fracture modes occurred by void formation at the Cr-dispersoids (E-phase). In the case of intergranular fracture, void coalescence was facilitated by the grain boundary η precipitates. The difference in fracture toughness behavior of these alloys has been shown to be dependent on the coarseness of matrix slip and the strength differential between the matrix and precipitate free zone (σ_M-σ_{PFZ}). A new fracture mechanism has been proposed to explain the development of the large amounts of intergranular fracture observed in the low toughness alloys.

I. INTRODUCTION

THE maximum attainable yield strength in the 7XXX series aluminum alloys (Al-Zn-Mg-Cu-Cr) can be extended from 517 MPa to 690 MPa by increasing the solute (Mg+Zn) content.[1] However, these ultra high strength alloys have very low fracture toughness values. This loss of toughness has been accompanied by an increased incidence of intergranular fracture. The mechanisms responsible for this loss of toughness with increasing solute content have not been satisfactorily defined due to several factors. Previous studies have typically not dealt with *isothermal* and *isochronal* comparisons. Therefore, any attempts to understand the singular role of the grain size,[2,3,4] precipitate free zone (PFZ),[5-8] grain boundary precipitates,[8,9] dispersoids,[2,4,10-19] or strengthening precipitates[2,3,8,12,20,21] have been overshadowed by other effects. For example, often while attempting to produce a change in the particular feature being investigated (*e.g.*, areal fraction of grain boundary precipitate), other microstructural variables were inadvertently altered through the heat treatment. In contrast, this research program was defined such that definitive critical evaluations could be made as to the role of the matrix microstructure* in determining fracture toughness. This was accomplished by altering the yield strength level of three alloys by increasing the solute content, but maintaining constant fabrication and aging conditions.

*The term "matrix microstructure" will be used to refer to the grain interior microstructure and includes the continuous, aluminum-rich α phase and the identity, volume fraction, and size of the strengthening precipitates exclusive of the dispersoids.

GERARD M. LUDTKA, formerly a Research Assistant at Carnegie-Mellon University, is now a Senior Research Engineer, General Motors Research Laboratories, Warren, MI 48090. DAVID E. LAUGHLIN is Associate Professor of Metallurgical Engineering and Materials Science, Carnegie-Mellon University, Pittsburgh, PA 15213.

Manuscript submitted May 11, 1981.

II. MATERIALS

Three compositions were selected to obtain a spectrum of yield strength values over which the fracture toughness could be monitored. These alloys differ from one another only in Mg and Zn contents. Hence, they have identical amounts of the ancilliary elements such as Cu, Cr, Ti, B, and Be which are normally used as alloy additions in the 7XXX series aluminum alloys. High purity base aluminum and alloying additions were used to produce these alloys to preclude the appearance of the large (0.1 to 30μm) Fe and Si bearing constituents which are generally present in commercial purity 7075 in amounts ranging from one to five vol pct. Previous studies[10,22] have shown that these inclusions are detrimental to fracture toughness and, consequently, that as their volume fraction and/or size is decreased, the fracture toughness is increased. The Fe and Si contents were each less than 0.01 wt pct in the final alloys.

A high purity version of a commercial 7075 composition was chosen as one of the three alloys. This serves as a reference whereby the normal yield strength level of approximately 504 MPa in the T6 temper is obtained. In addition, the relatively constituent-free microstructure would enhance fracture toughness. The 7075 aluminum alloy has 2.20 wt pct Mg and 5.59 wt pct Zn. This lowest Mg+Zn alloy will be referred to hereafter as the *low solute* alloy. The other two alloys have increasingly higher Mg and Zn contents and provide substantial increments in yield strength of 87 MPa and 118 MPa. These compositions will be referred to subsequently as the *intermediate solute* (2.81 wt pct Mg-6.96

ISSN 0360-2133/82/0311-0411$00.75/0

wt pct Zn) and *high solute* (2.76 wt pct Mg-7.84 wt pct Zn) alloys.

The chemical analyses of the three alloys chosen for this investigation are presented in Table I. Due to cracking of the ingot upon solidification, it was necessary to recast the *high solute* composition alloy; the recast version is referred to as heat B.

All three alloys were produced in sheet form and processed in an identical manner following procedures described elsewhere.[23] For this study only the T6 temper was investigated for the sheet materials. All of the alloys were solution treated for one hour at 471 °C (880 °F) and cold water quenched. They were stretched one to three pct to flatten, and aged for 24 hours at 121 °C (250 °F).

III. EXPERIMENTAL PROCEDURE

A. *Microstructure Characterization*

Optical metallography and transmission electron microscopy were used to characterize the microstructures in detail. The procedures and analytical techniques utilized are described elsewhere.[23]

B. *Mechanical Property Determination*

All of the tensile tests were performed using a 220 KN (50,000 pound) capacity MTS 810 Materials Test System at a strain rate of $4 \times 10^{-4} s^{-1}$ following the procedure outlined in ASTM E8–69.[24] Sheet specimens with a 25.4 mm gage length and 6.4 mm width were used.

The Kahn-type tear test[25-28] was chosen to evaluate the fracture toughness of the alloys. This test is a standard test used by the aluminum industry to monitor differences in toughness of sheet products. The tear tests were performed at a loading rate of 2,200 newtons per minute on the same equipment as the tensile data. Duplicate tear tests were conducted at the Alcoa Technical Center to determine the reproducibility of the tear data and to facilitate comparisons with existing Alcoa data on 7XXX aluminum alloys. Excellent agreement was obtained between the Alcoa generated data and that produced in this study, as will be shown in Table VII.

Another test which has been used extensively to characterize the fracture toughness of aluminum alloys[29-32] is the edge-notched tensile test. It is the ratio of the notched tensile strength to the yield strength that is used to evaluate toughness. This ratio is used primarily as a merit rating, since the values obtained depend on the notch design used. For this study, very sharp 60 deg V notches were used on 76 mm wide specimens.

R-curve analyses[33] were also performed for these alloys. To develop R-curves for all of the alloys in this investigation, 102 mm wide center cracked tension (CCT) panels were used. The testing procedure and analytic approach are thoroughly covered elsewhere.[34]

In addition to R-curves, plane-stress fracture toughness data, K_c, were determined from CCT panel data. K_c is the value of K_R at the instability condition determined from the tangency between the R-curve and the critical crack extension force curve of the specimen.[33]

Finally, the critical J-integral[35,36,37] values (J_c) were determined for these alloys. These were calculated from the P (load) *vs* v (load line displacement) plots obtained from the CCT panels. The estimation procedure used by Hickerson[38] on sheet material was followed to obtain the critical J-integral values.

C. *Fractography*

The fracture surfaces of the toughness specimens were examined in a JEOL JSM-35 Scanning Electron Microscope (SEM) operated at 25 KV. The relative amounts of intergranular fracture were determined utilizing a technique similar to that described elsewhere[23,34] for evaluating the volume fractions of constituents. The only difference is that the fraction, P_p, of total grid points lying on intergranular fracture features is now directly related to an areal rather than a volume measurement.

In addition, oxide replicas of fracture surfaces were evaluated using transmission electron microscopy. A Philips EM200 Transmission Electron Microscope operating at 80 KV was used. Oxide replicas were fabricated according to the technique outlined by Warke, *et al.*[39]

Measurements of intercept dimple spacings were made from these replicas using the same technique described for evaluating intercept grain sizes.[23] Similarly, dimensions of second phase particles associated with dimples on fracture surfaces were determined from these detailed oxide replicas.

D. *Slip Behavior Characterization*

The slip behaviors of these different alloys were characterized quantitatively from measurements made on prestrained tensile specimens ($\varepsilon_p = 0.02$) described in Reference 23.

X-ray microanalysis was performed on prestrained thin foils to identify the void-nucleating second phase particles. This analysis was performed by JEOL using a JEM 100CX TEMSCAN transmission electron microscope equipped with a Kevex TX7000 energy dispersive X-ray analyzer.

E. *Fracture Initiation*

For monitoring fracture initiation, thin foils were fabricated from prestrained tensile specimens and examined in the electron microscope.[40]

Table I. Chemical Composition Analysis (Wt Pct)

Alloy Designation	Si	Fe	Cu	Mg	Cr	Zn	Ti
Low solute	0.009	0.007	1.54	2.20	0.19	5.59	0.02
Intermediate solute	0.010	0.009	1.56	2.81	0.19	6.96	0.02
High solute A	0.010	0.009	1.48	2.74	0.19	7.74	0.02
High solute B	0.008	0.020	1.55	2.76	0.19	7.84	0.01

Note: Mn, Ni, B<0.01; Be<0.001.

To determine that voids observed at second phase particles did not result by selective attack during electrolytic polishing, several specimens from prestrained tensiles were ion milled. A comparison of the two techniques demonstrated that all of the observations and conclusions presented in the following sections about void initiation made from electrolytically thinned specimens could also be made from ion milled specimens. The voids observed, therefore, were not polishing artifacts. In addition, voids associated with second phase particles were not observed in thin foils made from unstrained samples.

IV. RESULTS

A. *Microstructure*

The quantitative microstructure data is summarized as follows. First, with the exception of the *high solute A* heat, the grain sizes of these alloys are identical. High solute A has a finer grain size. An optical micrograph exhibiting a typical microstructure is given in Figure 1. Table II summarizes the intercept grain sizes for these alloys. Second, due to the extreme high purity of these alloys (very low Fe and Si), the volume fraction of second phase constituents (inclusions) is negligible (<0.017 vol pct). This enables an evaluation of the matrix toughness properties without having to be concerned about inclusions initiating fracture prematurely and hence overshadowing the inherent matrix properties.

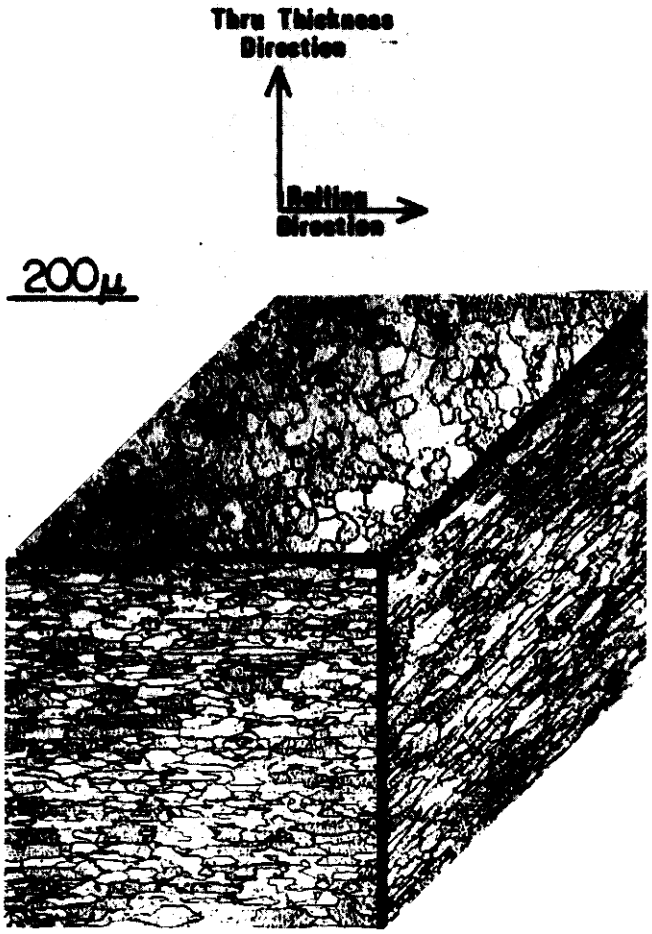

Fig. 1 — Typical optical micrograph of the 1.6 mm sheet alloys investigated in the T6 temper.

Table II. Intercept Grain Sizes*

Alloy	Longitudinal Direction (a) (μm)	Long Transverse Direction (b) (μm)	Short Transverse Direction (c) (μm)
Low solute	38.9 ±2.3	35.0 ±2.1	17.3 ±0.6
Intermediate solute	35.3 ±1.8	34.9 ±1.5	16.4 ±0.7
High solute A	25.5 ±2.0	23.7 ±1.3	14.2 ±1.2
High solute B	35.9 ±3.8	34.6 ±3.0	16.3 ±0.7

(a) Rolling direction
(b) In the rolling plane but perpendicular to the rolling direction
(c) Through the thickness direction

* Data indicate the mean ±one standard deviation.

Tables III through V list the quantitative TEM data generated in this study for the precipitate free zones, dispersoids, and grain boundary precipitates. In addition, the average size of the matrix precipitates was found to be approximately 40Å (with a spread between 20Å and 75Å). Figure 2 exhibits representative features observed during examination of thin foils in the TEM for these alloys. An important observation to make is that there exists a significant difference between the values of the average effective

Table III. Precipitate Free Zone (PFZ) Widths*

Alloy	PFZ Width Å
Low solute	280 ±29
Intermediate solute	269 ±31
High solute A	280 ±17
High solute B	267 ±31

* Data indicate the mean ±one standard deviation.

Table IV. TEM Quantitative Data for *E*-Phase Dispersoids*

Alloy	$\bar{d}_D$ (nm)	$\bar{\lambda}_D$ (nm)	$\bar{N}_v$ (in 10^{13} Particles/cm^3)	Vol Pct**
Low solute	79 ±37	189 ±12	2.57 ±0.46	0.663
Intermediate solute	83 ±58	200 ±16	2.19 ±0.50	0.656
High solute	81 ±42	198 ±13	~~2.19 ±0.50~~ 2.26±0.57	0.629

* Data indicate the mean ±one standard deviation.
** Calculated using the mean values for $\bar{d}_D$ and $\bar{N}_v$.

Table V. TEM Quantitative Data for Grain Boundary η Precipitates*

Alloy	$\bar{d}_p$ (nm)	$\bar{\lambda}_p$ (nm)	$\bar{N}_A$, Precipitates/μm^2	Areal Pct f_p**
Low solute	20 ±2	25 ±2	392 ±40	14
Intermediate solute	20 ±1	27 ±3	336 ±51	15
High solute	25 ±2	26 ±3	357 ±43	18

* Data indicate the mean ±one standard deviation.
** Calculated using the mean values for $\bar{d}_D$ and $\bar{N}_v$.

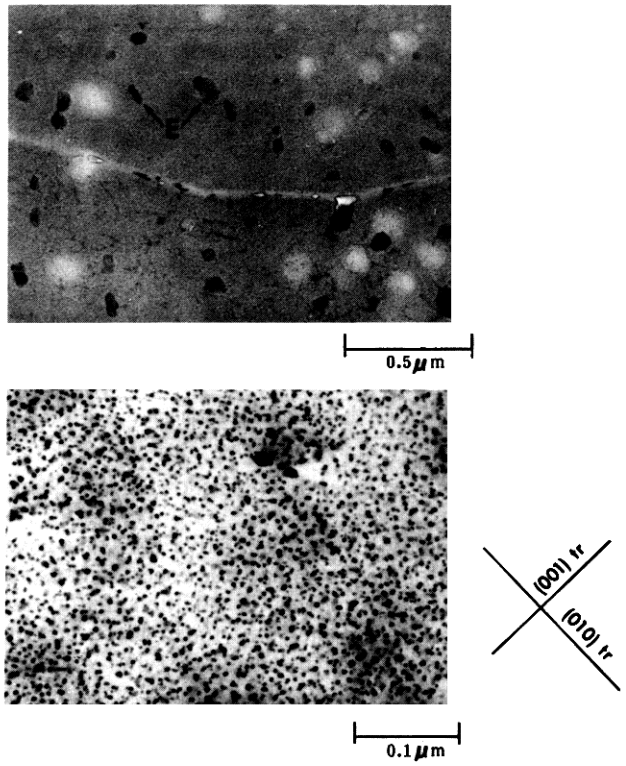

Fig. 2(a), (b)—Typical multiple beam, bright field TEM micrographs exhibiting microstructural features representative of the compositions studied in the T6 temper. "*E*" indicates the Cr-dispersoid.

dispersoid diameter, $\bar{d}_D$, and the average grain boundary precipitate diameter, $\bar{d}_\rho$, as well as between the average dispersoid spacing, λ_D, and the average grain boundary precipitate interplanar spacing, λ_ρ, (refer to Tables IV and V). This fact will be essential in determining which microstructural entity is responsible for fracture initiation.

B. *Tensile Flow Characteristics*

These alloys were tested in uniaxial tension to document the yield strength increase in the T6 temper by increasing the amount of solute addition. Flow curve parameters were determined for two different curve fit forms and are summarized along with the other pertinent tensile test data in Table VI.

Several trends can be seen in the data presented in Table VI. First, as the solute content is increased, the yield strength in the T6 temper is increased from the commercially available value of approximately 496 MPa (72 ksi) to almost 621 MPa (90 ksi). This represents a 25 pct increase. Hence, this would be extremely beneficial for weight saving design purposes if other properties such as fracture toughness could be enhanced. Conversely, the work hardening exponents, n_1 and n_2, and all three strain parameters, ε_u (uniform elongation), ε_f (true tensile fracture strain), and pct elongation, are seen to decrease as the solute content increases (or as the yield strength increases for the T6 temper).

C. *Fracture Toughness Data*

The results from all of the toughness tests are listed in Table VII. Figure 3 exhibits the K_R curves (K *vs* Δa_e) obtained from the CCT panels. Since only 102 mm wide panels were used, only a portion of the K_R curve could be obtained. These curves could be extended further (along Δa_e) if wider material were tested. Critical J-integral data are plotted *vs* yield strength in Figure 4 to demonstrate graphically the dramatic loss of toughness with increasing yield strength. As these alloys were available in an unrecrystallized microstructure *via* 12.7 mm thick plate, 1.6 mm thick tear specimens were milled out of the plate center and unit propagation energies determined. The results of these tests are shown in Figure 5. They demonstrate that an uncrystallized microstructure, for the same composition and heat treatment as its recrystallized counterpart, can maintain higher toughness at a higher yield strength.

D. *Fractography*

Since the fracture topographies of the *intermediate* and *high solute* alloys were equivalent, only the *low* and *high solute* alloys will be discussed in this section. Any generalities made for the *high solute* alloy can be taken, without exception, as pertaining to the *intermediate solute* alloy, also.

The *low solute* alloy fracture surfaces were always slant fractures at an angle of approximately 45 deg from the rolling plane and loading axis. Slight necking occurred in the crack tip region. The slanted nature of the crack front

Table VI. Mechanical Properties*

Alloy	σ_{ys} 0.2 Pct Yield Strength (MPa)(a)	Ultimate Tensile Strength (MPa)(a)	True Fracture Stress (MPa)(a)	Uniform Elongation ε_u	Tensile Fracture Strain ε_f	Pct Elongation (in 25.4 mm Gage Length)	K_1 (MPa) (a)(b)	n_1 (b)	σ_0 (MPa) (a)(c)	K_2 (MPa) (a)(c)	n_2 (c)
Low solute	496 ±0.7	551 ±2.1	672 ±9.7	0.123 ±0.006	0.278 ±0.020	16.23 ±0.17	718	0.070	490	549	0.680
Intermediate solute	583 ±2.8	627 ±2.1	773 ±9.7	0.114 ±0.001	0.247 ±0.017	15.10 ±0.35	790	0.058	576	518	0.657
High solute A	614 ±0.7	654 ±1.4	781 ±4.1	0.102 ±0.000	0.212 ±0.010	14.80 ±0.57	815	0.054	605	491	0.631
High solute B	602 ±1.4	643 ±1.4	771 ±7.6	0.097 ±0.007	0.210 ±0.013	14.10 ±0.67	802	0.054	595	496	0.639

(a) 1 ksi = 6.9 MPa
(b) Flow curve parameters for the form $\sigma = K_1\varepsilon^{n_1}$.
(c) Flow curve parameters for the form $\sigma = \sigma_0 + K_2\varepsilon^{n_2}$.

* Data indicate the mean ±one standard deviation where applicable.

Table VII. Fracture Toughness Data – LT Orientation*

Alloy	σ_{ys} 0.2 Pct Yield Strength (MPa)(a)	Tear Strength (MPa)(a)	Unit Propagation Energy (J/mm^2)	Notched Tensile Strength (MPa)(a)	Plane Stress Fracture Toughness,** K_c ($MN/m^{3/2}$)(c)(d)	Critical J Integral, J_c (J/mm^2)(b)
Low solute	496 ±0.7	704 ±2.8 (705 ±14.0)[e]	0.157 ±0.015	522 ±26.2	102.3 ±1.8	0.107 ±0.004
Intermediate solute	583 ±2.8	629 ±8.3 (618 ±42.8)[e]	0.011 ±0.003 (estimated)[f]	362 ±2.1	52.4 ±0.1	0.038 ±0.000
High solute A	614 ±0.7	515 ±39.3 (507 ±11)[e]	0 (rapid fracture)[f]	329 ±9.0	36.1 ±1.8	0.018 ±0.001
High solute B	602 ±1.4	560 ±35.9 (529 ±11.7)[e]	0 (rapid fracture)[f]	345 ±0.7	38.6 ±0.9	0.021 ±0.001

(a) 1 ksi = 6.9 MPa.
(b) 1 in-lb/in^2 = 1.75×10^5 ergs/cm^2 = 1.75×10^{-4} J/mm^2.
(c) 1 ksi$\sqrt{\text{in}}$ = 1.1 MN/m$^{3/2}$.
(d) Determined by R-curve analysis of 102 mm wide center cracked tension panels.
(e) Generated by Alcoa.
(f) Curves not reliable due to rapid fracture; therefore, energy may be near zero.

* Data indicate the mean ±one standard deviation.
** K_c = 69.0 ksi $\sqrt{\text{in.}}$ for commercially available 7075-T6, 0.063 inch sheet [1].

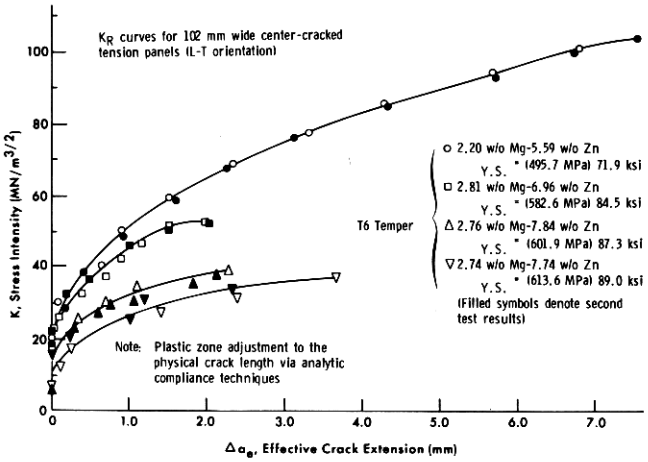

Fig. 3—R-curve plots from 102 mm wide center cracked tension (CCT) panels.

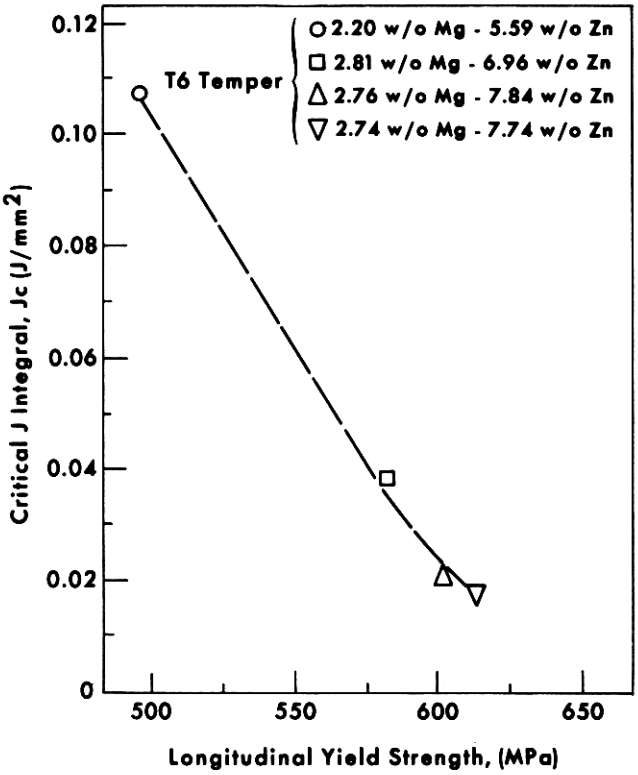

Fig. 4—Critical J integral values, J_c, as a function of yield strength.

and the necking resembled Mode III separation (through thickness shearing) previously observed in sheet materials. Some buckling of tear test specimens for the *low solute* alloy was observed during the testing.

The *high solute* alloy fracture surfaces were predominantly square, *i.e.*, approximately 90 deg to the rolling plane and loading axis. However, near the sheet surfaces small slant fracture regions did occur which are indicative of some through-thickness shearing.

Examination of the fracture surfaces in the SEM revealed extremely different fracture topographies for the *low* and *high solute* alloys, as shown in Figure 6. The *low solute* alloy fracture (Figure 6a) was predominantly transgranular dimpled rupture, while the *high solute* alloy (Figure 6b) appeared to fail by a predominantly intergranular fracture mode. A very fine population of dimples of uniform size is evident on the *low solute* alloy fracture surface (Figure 6a). Occasionally some slightly larger dimples are seen (probably due to the few Fe and Si constituents in this alloy). Several interesting features are evident on the fracture surface of the *high solute* alloy (Figure 6b). First, although the fracture is predominantly intergranular, there are isolated transgranular ligaments evident on the fracture surface that must be explained. Also, fissures extending down along grain boundaries parallel to the loading direction and perpendicular to the fracture surface are evident and tend to bracket the transgranular ligament regions. Only occasionally are some regions of shear across an entire grain width observed.

Very small particles (~0.1 μm) were found to be associated with the fine dimples (Figure 7) in the transgranular

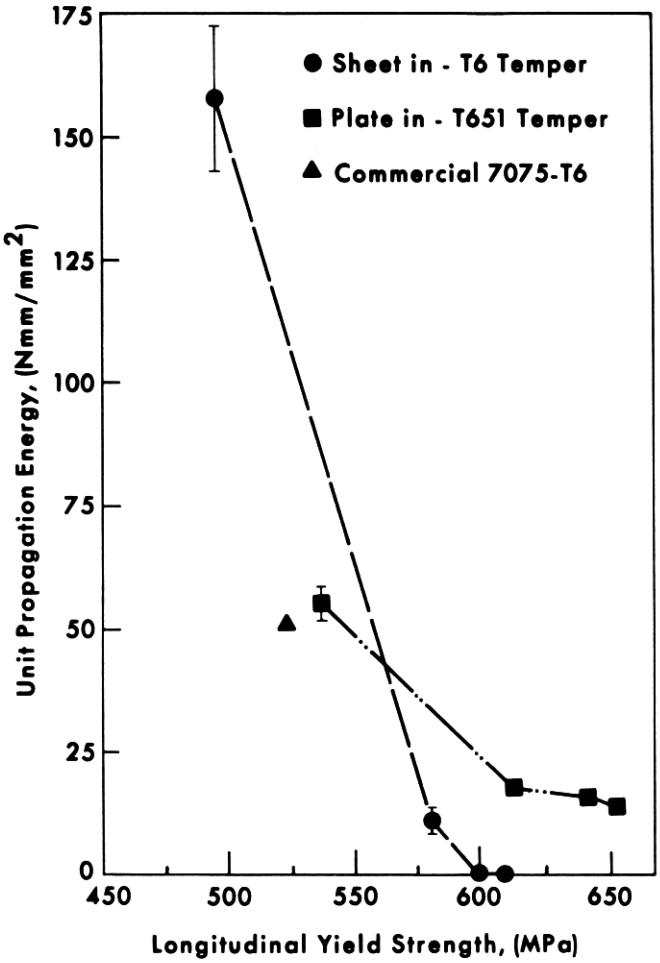

Fig. 5 — Unit propagation energy *vs* yield strength plot.

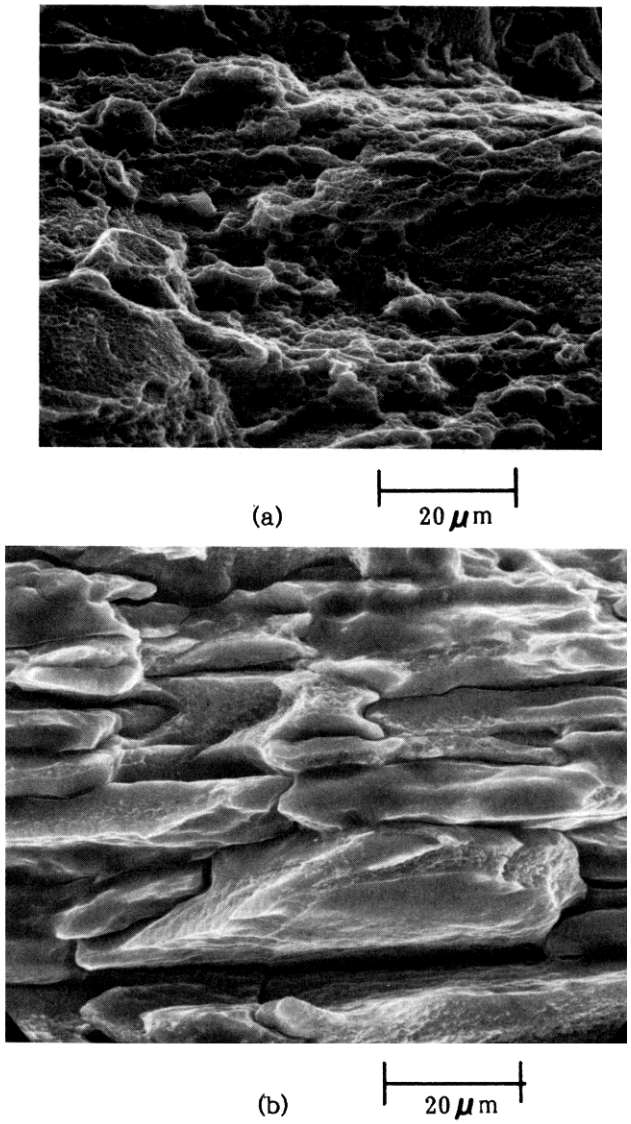

Fig. 6 — Scanning electron fractographs of Kahn-type tear specimens. (*a*) *low solute* alloy; (*b*) *high solute* alloy.

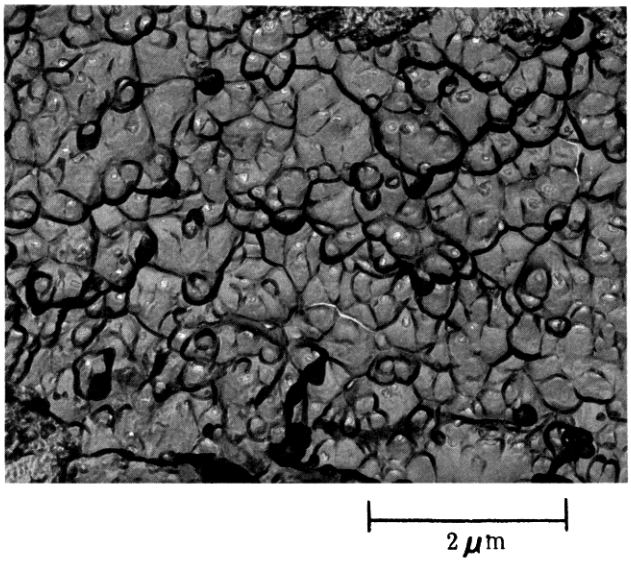

Fig. 7 — TEM fractograph of an oxide replica exhibiting typical transgranular dimples observed in both *low* and *high solute* alloys.

fracture regions for both the *low* and *high solute* alloys when oxide replicas were viewed in the TEM. The size and shape of these particles are very similar to those of the Cr-dispersoid (E-phase). Although not evident in the SEM fractographs, small features became evident on all of the grain boundaries of the *high solute* alloy (Figure 8a). In addition, at much higher magnification (Figure 8b) the fracture mode of the *high solute* alloy is revealed to be predominantly intergranular dimpled rupture. Very shallow dimples with fine particles (~0.1 μm) can be distinctly discerned. Some of these dimples were elongated, suggesting that grain boundary shear occurred. The occasional intergranular facet seen in the *low solute* alloy had comparable features.

Quantitative fractography was performed to facilitate correlations between the microstructure of these alloys and fractographic features. For this purpose the mean intercept dimple sizes as well as the average dimple-nucleating particle diameters were measured for both the transgranular and intergranular fractures. Since the dimple sizes of the transgranular regions of both the *low* and *high solute* alloys were comparable, only one set of values for each feature is presented in Table VIII. The relative amounts of intergranular fracture for all the alloys in the T6 temper were also determined to document any trend in loss of toughness accompanying increased amounts of intergranular fracture.

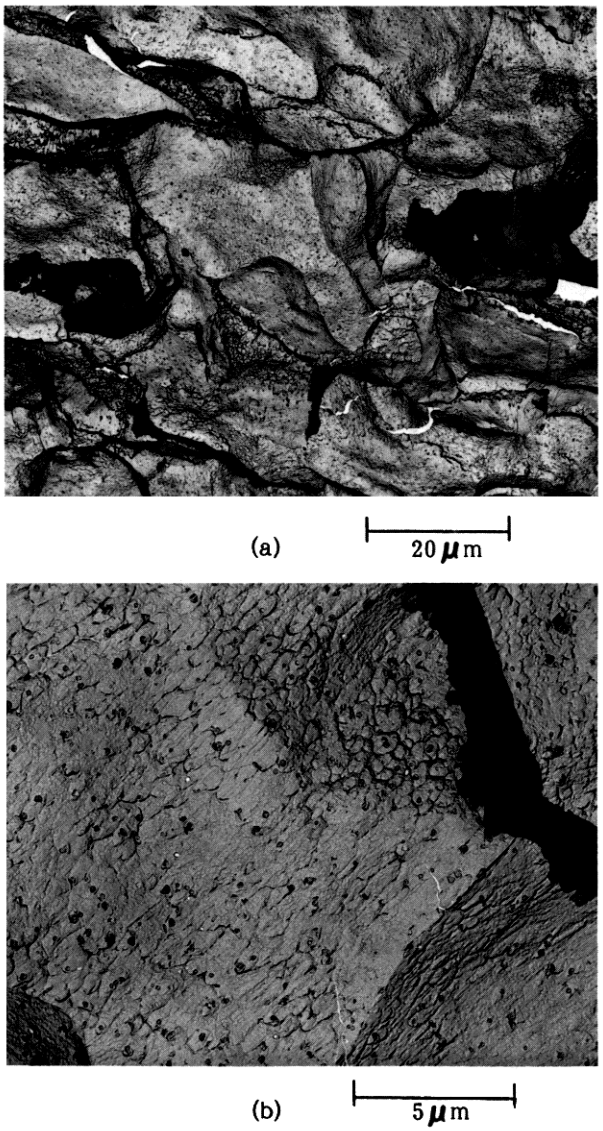

Fig. 8—TEM fractographs of oxide replicas of the *high solute* alloy, showing the predominately intergranular dimpled rupture nature of the fracture.

These data are tabulated in Table IX. Comparison of the values in Tables VIII and IV shows excellent correlation of the transgranular and intergranular dimple data with that of the Cr-dispersoid population. Several factors should be noted. First, the measured average transgranular dimple spacing and particle diameter would be expected to be larger than the measured matrix interparticle spacings and sizes for the Cr-dispersoid, since the larger dispersoids would be expected to initiate fracture first. Thus, not all of the dispersoids in an area could contribute to the final fracture process. Similarly, since the dispersoid data in Table IV are based on volume measurements while a grain boundary is only two dimensional, the mean interplanar dispersoid spacing on the boundary would naturally be larger than a volume interparticle spacing. This is because not all nearest neighbors are accounted for in a plane boundary. Hence, the initiation for both the transgranular and intergranular dimpled rupture fracture modes has been indirectly correlated with the E-phase (Cr-dispersoid).

Table VIII. Quantitative Fractography Results – I*

	Transgranular Fracture	Intergranular Fracture
Mean intercept dimple size (nm)	316 ±42	331 ±77
Dimple nucleating particle average diameter (nm)	102 ±47	174 ±66

* Data indicate the mean ±one standard deviation.

Table IX. Quantitative Fractography Results – II*

Alloy	Intergranular Fracture Pct Areal Fraction
Low solute	2.4 ±2
Intermediate solute	69.2 ±6.1
High solute A	72.9 ±5.3
High solute B	71.6 ±4.4

* Data indicate mean ±one standard deviation.

E. *Crack Tip Examinations*

Tear test specimens were pulled in tension such that a crack was initiated and had begun to propagate. The test was stopped before unstable crack growth led to catastrophic failure. The crack tip region was cut out of the specimen and mounted such that the plane of polish would be normal to the plane of crack propagation. This enabled examination of the crack tip region itself. Specimens were polished until only a portion of the crack tip was visible. This meant that the ends of the visible crack and beyond were at or just ahead of the physical crack tip and could give information regarding the fracture initiating event. Calculations of the minimum plastic zone size, r_ρ, from the plane stress toughness values demonstrate that even for the smallest zone size of 0.55 mm (at least 15 grain diameters), material at a substantial distance ahead of the crack is contained in the plastic

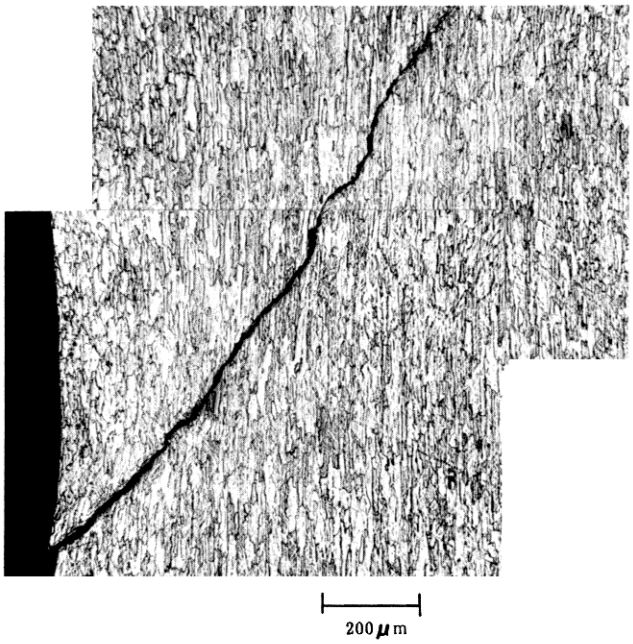

Fig. 9—Optical micrograph of the crack tip region in the *low solute* alloy viewing the crack head-on.

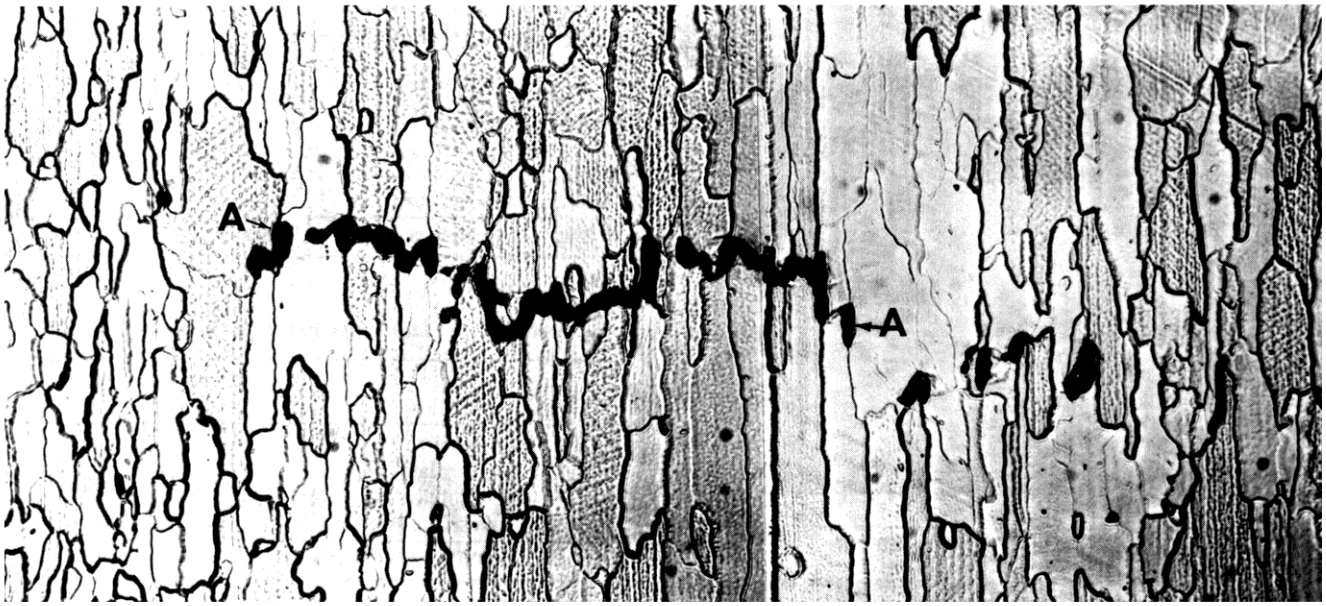

Fig. 10 — Optical micrograph of the crack tip region in the *high solute* alloy, viewing the crack head-on. Areas marked "A" indicate intergranular separation.

zone associated with the crack tip. Hence, this provided valuable information regarding the fracture process.

For the *low solute* alloy (Figure 9) the fracture mode is predominantly transgranular with the crack path only occasionally following a grain boundary. The observation of deformation extending from the crack tip in a direction approximately 45 deg to the tensile axis supports the idea that the fracture path initiates in and follows a plane of maximum macroscopic shear stress (for a sheet specimen in plane stress). Since the volume fraction of Fe and Si constituents is extremely small, the fracture path is not controlled by these particles. Normally in commercial 7075 alloy products, fracture initiates by void nucleation at the larger constituents and void sheets are seen to form between these larger voids along planes of maximum shear stress.[19]

Several interesting observations can be made upon examination of the crack tip region of the *high solute* alloy (Figure 10). First, as mentioned before, the plane of the crack is normal to the tensile loading direction (*i.e.*, a square profile). This type of fracture appearance is usually seen under conditions of plane strain. Second, the regions where the crack tip has already passed by appear to have failed transgranularly. This is not in agreement with the quantitative fractography results (~70 pct intergranular fracture). Close examination, however, reveals that this initial observation is misleading. By looking at those points marked "A" in Figure 10, the conclusion can be made that intergranular separation occurs first. These voids along the grain boundaries can then grow even in a direction parallel to the loading direction — possibly assisted by the σ_3 stress.

Due to the loss of constraint by the adjacent grains, a grain is now free to deform as an individual ligament, and necking and shearing are observed to occur which rotate the grain boundaries inward and form the final transgranular ligament at the reduced neck. This explains the intergranular fissures parallel to the loading axis as well as the isolated transgranular ligaments discussed in the fractography section. For this conclusion to be consistent with the actual fracture topography, the mating grain boundary surfaces should be seen separated from each other but on the same fracture half — not on the mating fracture half. The SEM fractograph in Figure 11 exhibits this type of correlation, as

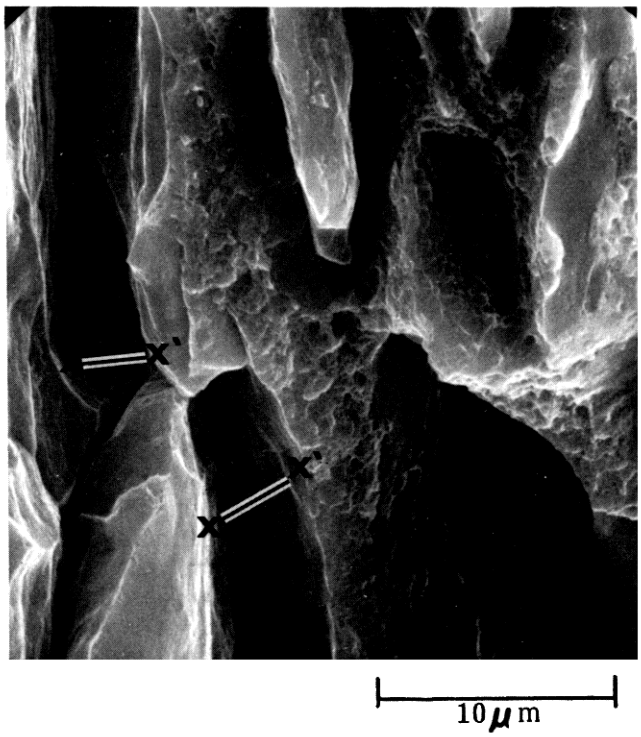

Fig. 11 — Scanning electron fractographs of the *high solute* alloy. Matching features are marked as X and X′.

is noted by the variously marked matching features. This observation of and explanation for the intergranular fracture with associated transgranular ligaments has never been suggested before to explain the fracture topography in 7XXX series sheet alloys. Occasionally regions of shear dimples spanning an entire grain width are observed. These are indicative of a grain favorably oriented for shear failure. Therefore, some (few) transgranular regions are visible that do not arise from the ligament mechanism described above.

There are other regions, as observed fractographically, where grain boundaries are oriented favorably to the tensile axis. Here grain boundary shear can occur, giving rise to an intergranular facet free from a transgranular ligament. Evidence of grain boundary shear on a boundary oriented 45 deg to the tensile axis is seen in Figure 12. Here the displacement of fiducial marks scratched onto a lightly etched, electropolished tensile specimen ($\varepsilon_p = 0.02$) is visible across a grain boundary. Similarly, a grain facet without any transgranular ligaments could form if the grain boundary was favorably oriented for the continuation of an already initiated intergranular or shear crack.

Slip Character: This characterization was the topic of another paper,[23] and therefore only the conclusion will be presented here. All of the alloys exhibited planar slip for $\varepsilon_p = 0.02$. The slip in the higher solute alloys was coarser as determined from slip band spacing and slip step height measurements. This tendency toward more strain localization with higher solute levels was shown to be directly related to the increase in volume fraction of the matrix precipitates.

Traces of slip bands were visible on the occasional intergranular facets seen on the fracture surface of the *low solute* alloy (Figure 13) and provide evidence of grain boundary accommodation of the matrix slip. One mechanism for void formation at grain boundary – slip band intersections which would lead to intergranular fracture will be presented at the end of this section.

Examination of foils at higher strains (seven pct and near-fracture strains) revealed the onset of more homogeneous deformation, *i.e.*, the areas between the initial slip bands begin to develop, qualitatively speaking, a homogeneous dislocation distribution.

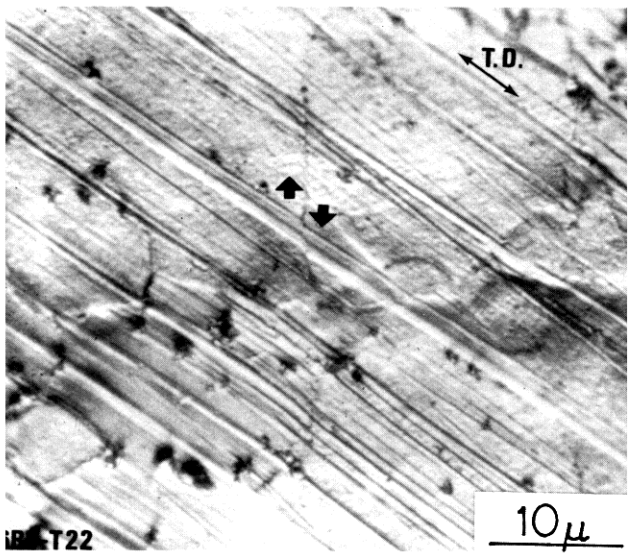

Fig. 12—Optical micrograph of the *high solute* alloy showing grain boundary shear (at arrows). "T. D." indicates tensile loading direction.

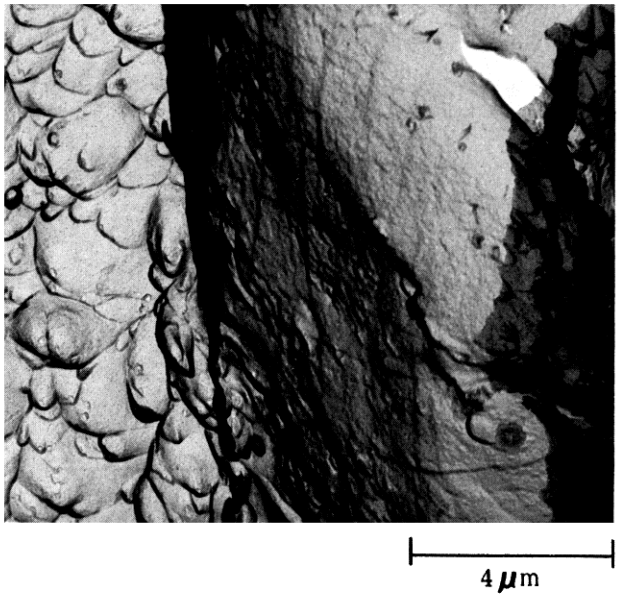

Fig. 13 — TEM fractograph of a replica from the *low solute* alloy showing slip band traces on an intergranular facet.

Void Initiation: To observe *in situ* void initiation, thin foils made from tensile specimens strained to approximately seven pct and near-fracture were examined in the TEM.

At seven pct strain, several cleaved matrix dispersoids were apparent in the *low solute* alloy (Figure 14). Fracture of a larger number of matrix dispersoids was evident at $\varepsilon_p = 0.23$.

Several interesting observations were made upon examining thin foils of the *high solute* alloy. At the seven pct strain level there was evidence of a few cleaved matrix dispersoids. In addition, several dispersoids with internal microtwins were observed (Figure 15a). However, the predominating number of voids were associated with the grain

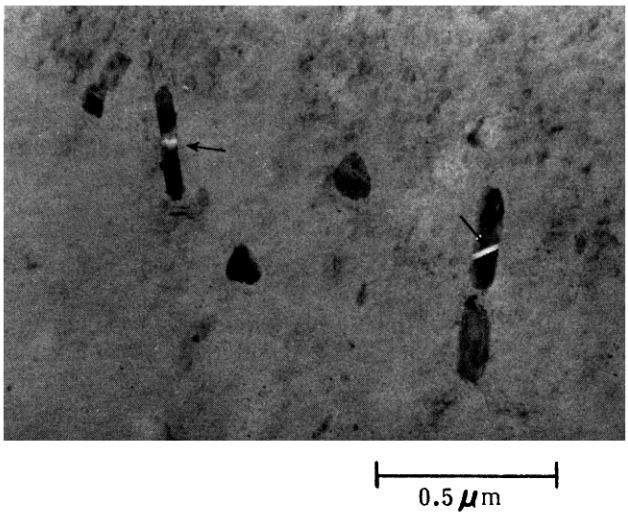

Fig. 14 — Examples of void initiation in a prestrained tensile specimen of the *low solute* alloy at $\varepsilon_p = 0.07$. The arrow indicates void initiation at a Cr-dispersoid.

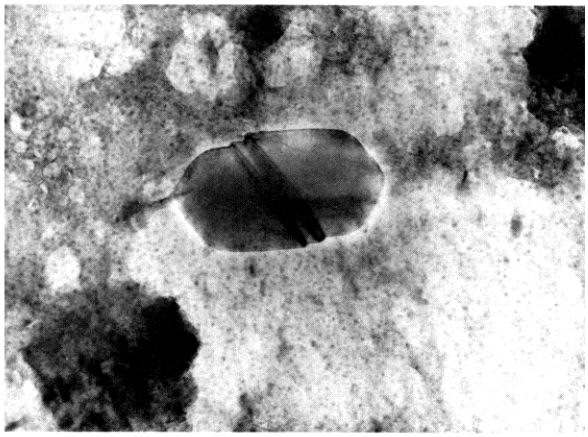

Fig. 15—(*a*) An internally microtwinned Cr-dispersoid (*E* phase). (*b*) Example of void initiation in a prestrained tensile specimen of the *high solute* alloy at $\varepsilon_p = 0.07$ ("v" designates a void).

boundary Cr-dispersoids (Figure 15b). STEM microchemical analysis performed on the particles associated with grain boundary voids directly identifies them as the Cr-dispersoid. These particles are not the grain boundary precipitate η, as previously suggested.[8] The results of this analysis are shown in Figure 16. The data, obtained using a Kevex attachment on a STEM, unequivocally show that the particles associated with a void have a strong Cr peak (Figure 16b). The smaller particles are shown to be richer in Mg and Zn than the matrix (Figures 16c, d) and exhibit no Cr peak, as would be expected of the η precipitate.

At a $\varepsilon_p = 0.21$, virtually every grain boundary dispersoid (*E*-phase) has a void associated with it, and void initiation at some of the grain boundary η-precipitates had occurred. As is shown in Figure 17a, final intergranular separation is facilitated by the growth and eventual coalescence of these intergranular voids. Triple points are also observed to act as sites for void initiation at this strain level and are probably the result of grain boundary shear. A significant portion of the matrix dispersoids (Figure 17b) have voids associated with them. This void formation is always associated with

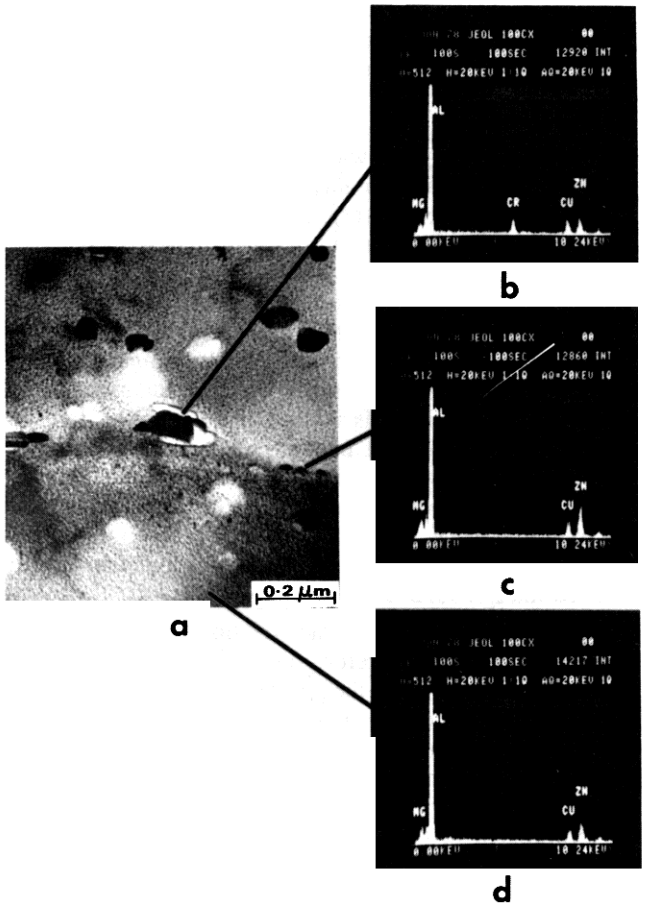

Fig. 16—X-ray microanalysis identifying the Cr-dispersoids as the intergranular fracture void nucleating particles.

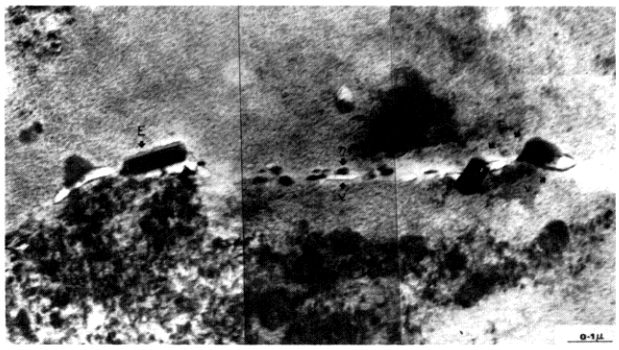

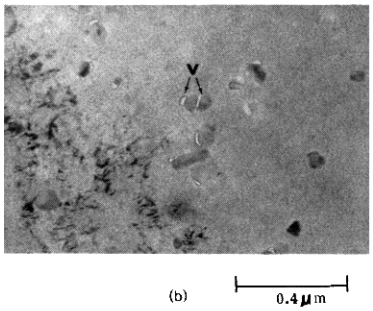

Fig. 17—Bright field TEM micrographs from a prestrained tensile specimen of the *high solute* alloy at $\varepsilon_p = 0.21$ ("v" designates a void and "E" indicates a Cr-dispersoid). (*a*) Grain boundary region; (*b*) matrix area adjacent to grain boundary in "a."

dispersoid cleavage or the decohesion of matrix-dispersoid interfaces. After the grain boundary has failed, these voids assist the formation of the transgranular ligament observed on the fracture surface of the higher solute alloys.

As mentioned earlier in this section, a mechanism for void formation at grain boundary–slip and band intersections will now be demonstrated. Figure 18 depicts such a mechanism, as observed in the *high solute* alloy at the higher strain level ($\varepsilon = 0.21$). The slip behavior in this alloy was shown previously to be planar. With increasing strain levels these slip bands produce more strain localization at their point of impingement on the grain boundary. The boundary must somehow accommodate this strain. One such way is for the boundary to deform, as is shown in Figure 18a within the circled region. The adjacent grains, however, have been significantly strengthened by the higher solute content and offer constraint and resistance against the grain boundary deforming. If this constraint is significant enough and there is a weaker path to relieve this strain, such as the precipitate-free zone (PFZ), void initiation will result in the PFZ at sufficiently high strain levels. This has been observed in Figure 18b, where a void is seen to nucleate at the point of intersection of a slip band and the grain boundary. In this case, void initiation was facilitated by the presence of a grain boundary Cr-dispersoid. Stresses normal to the boundary or in its plane would assist the growth of this void along the boundary. By linking up with similar voids, this would lead to the final intergranular dimpled rupture fracture observed.

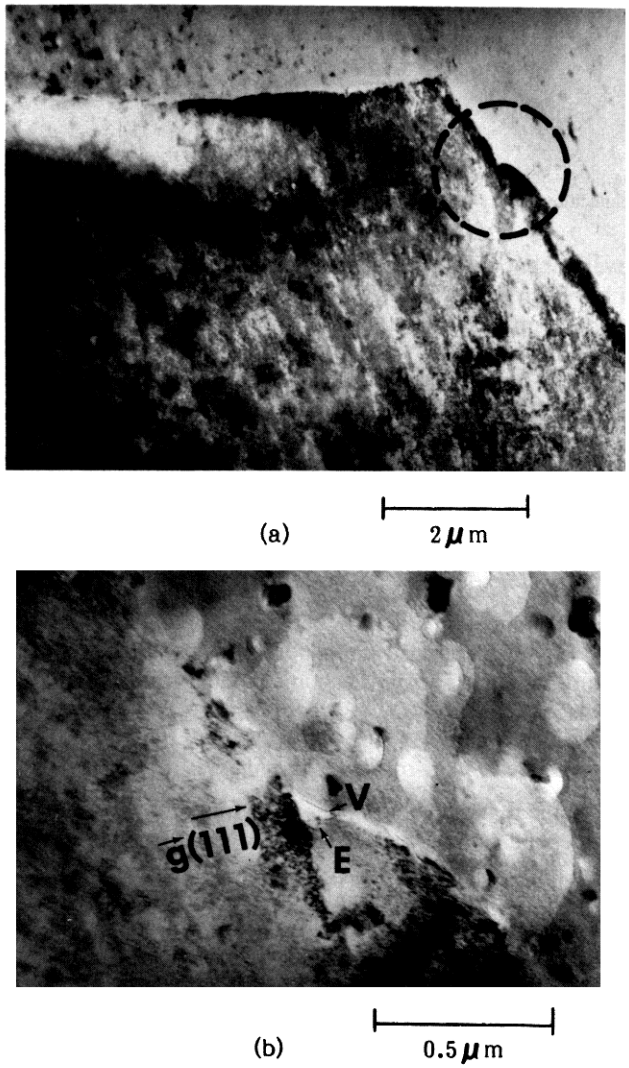

Fig. 18—(*a*) Bright field TEM micrograph from a prestrained tensile specimen of the *high solute* alloy at $\varepsilon_p = 0.21$; (*b*) higher magnification view of encircled region in part (*a*) ("v" designates a void, and "E" indicates a Cr-dispersoid).

V. DISCUSSION

A. *Microstructural Effects*

The three alloys being investigated in this study have been shown to be identical in every microstructural feature except that in the T6 temper the volume fraction (*i.e.*, number per volume; the sizes are the same) of the fine G.P. + η' precipitates increases with increasing solute content. The *low solute* alloy has the highest fracture toughness and the lowest yield strength in the T6 temper. Conversely, the higher solute alloys exhibit higher yield strengths but lower fracture toughness values. Differences in fracture behavior are discussed below.

In the *low solute* alloy, the fracture mode is transgranular dimpled rupture and follows the microscopic maximum shear planes through the thickness direction, resulting in a slant-type fracture. The E-phase (Cr-dispersoids) has been determined *via* quantitative fractography and quantitative TEM to be responsible for void initiation in this alloy. Previous studies[10,11] have already shown that the fine transgranular dimples in 7XXX alloys were due to these dispersoids.

The fracture in the *high solute* alloy is predominantly (~ 70 pct) intergranular dimpled rupture, and the fracture surface is square rather than slant. However, isolated, narrow transgranular ligaments as well as intergranular fissures parallel to the loading axis are visible. Examining the crack tips head on *via* optical metallography reveals that the presence of both of these fractographic features is due to longitudinal intergranular cracks opening up. This process is followed by the necking down of the individual grains until their final fracture results in the final transgranular ligament.

Price and Kelly,[41] on testing single crystals of Al-Cu, Al-Ag, and Al-Zn, have observed that these single crystals also neck down to a fine chisel edge (transgranular ligament) when aging is beyond the G.P. zone stage. When G.P. zones are primarily present, nearly-planar surface fractures parallel to an operative slip plane result. Hence, for the higher solute alloys, which are aged past G.P. zones alone, it appears that once these intergranular, longitudinal cracks form, the unconstrained grains deform as precipitation hardened single crystals do. Just as the constraint of adjacent grains helps produce a much higher yield strength in a polycrystalline aggregate than obtainable in single crystals alone (Taylor[42] analysis), it is anticipated that the lack of constraint of these grains after intergranular fracture occurs would result in a lower fracture toughness. This idea of ligament formation, as described, has never been cited in the literature for these alloys before.

The implications of this mechanism are important. First, the fracture surfaces appear to be ~ 70 pct intergranular fracture. This apparent fracture mode, however, obscures

the true total fracture process. In fact, the ~ 30 pct remnant transgranular fractures are the result of the individual grains necking down and exposing more intergranular features (and, therefore, more apparent intergranular fracture) until the final chisel edge formed. Realizing this enables an obvious conclusion to be reached. That is, the matrix properties are very important in determining the final fracture toughness, and not only the grain boundary properties, as so frequently suggested. This conclusion helps explain the difference in toughness between the *intermediate* and *high solute* alloys. Both have the same amount of apparent intergranular fracture, yet the *intermediate solute* alloy has a plane stress fracture toughness of 53.3 $MNm^{-3/2}$ (47.6 ksi$\sqrt{in}$), while the *high solute* alloy has a value of only 38.2 $MNm^{-3/2}$ (35.1 ksi$\sqrt{in}$). If only the grain boundary properties were critical, then these values should be closer. Evidently, then, the response of the matrix to the applied stress field as a function of differences in only volume fraction of the strengthening precipitate is the reason for the observed difference in toughness. It should be noted that evidence of intergranular fracture from grain boundary shear alone, as well as an occasional region of transgranular fracture (approximately the width of a grain) were observed.

Similar to the *low solute* alloy, the fine transgranular dimples in the higher solute alloys are formed *via* void formation at the fine E-phase (Cr-dispersoids). However, contrary to suggestions in the literature,[8] the intergranular dimples have been shown to be formed at the grain boundary dispersoids, and not the coarse grain boundary η precipitates. This has been unquestionably proven by observations of void nucleation at these E-phase particles in prestrained tensile specimens. Exact identification of the void nucleating particles involved microanalysis performed using a KEVEX attachment on a STEM. Similarly, data from quantitative transmission electron microscopy isolate the Cr-dispersoid as the void-nucleating particle. This research has further demonstrated that the grain boundary η precipitates facilitate void coalescence and final fracture of the grain boundaries. In cases, then, where intergranular fracture is due solely to grain boundary shear, the areal fraction of grain boundary precipitate is important, since the void coalescence stage is accelerated with higher areal fractions. This is observed on very coarse grained, equiaxed microstructures.[9]

This research has quantitatively shown that the slip is coarser in the higher solute alloys than in the *low solute* alloy. That is to say, that the slip bands are farther apart and have larger offsets associated with them in the *high solute* alloy. Therefore, at the point of impingement of a slip band with a grain boundary, there is more strain localization at a given macroscopic strain level for the *high solute* alloy than for the *low solute* alloy. Void formation at the grain boundary results, as shown in Figure 18b, at a grain boundary dispersoid. Fracture of grain boundaries due to the intersections of slip bands with the boundary has been observed by Gysler, *et al*,[43] in a Ti-Mo alloy, by Lutjering and Weissman[44] in Ti-Al alloys, and by Evensen, *et al*[45] in Al-Mg-Si alloys. However, this intergranular fracture was not associated with any transgranular ligament formation. This means of void formation was used to describe the mechanism responsible for the intergranular fracture occurring in the high solute alloys. Figure 19 pictorially depicts the sequence of events responsible for the development of the final fracture in the higher solute alloys, as has been determined by this research.

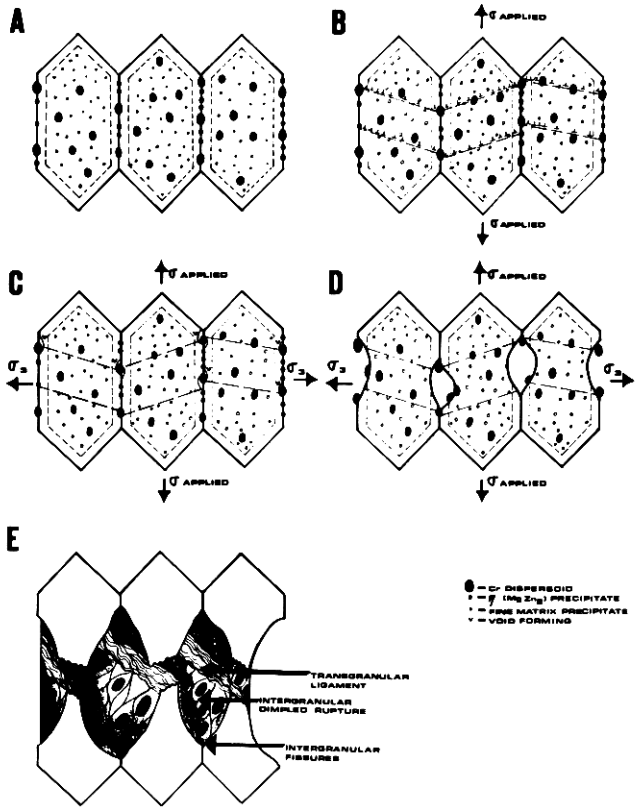

Fig. 19 — Schematic of the sequence of events during fracture of the high solute alloys.

Coarse matrix slip, as in the higher solute alloys, therefore leads to lower toughness values. A work softening model of Hornbogen and Gahr[46] has been shown elsewhere[23] to predict the difference in strain localization observed for these alloys. In this model the tendency toward coarser slip is correlated directly to the volume fraction, f, of matrix precipitates and inversely with precipitate diameter, d, *i.e.*,

$$\text{More coarse slip or greater work softening} \propto \frac{f^{1/3}}{d} \qquad [1]$$

The difference in strength between the matrix and the PFZ, $(\sigma_M - \sigma_{PFZ})$, is also an important factor in the overall fracture scheme. This will become evident from the following discussion.

B. *Influence of* $(\sigma_M - \sigma_{PFZ})$ *on Toughness*

Assume that the solution has been found in which toughness depends on slip behavior alone, that is, inhibit coarse slip in these alloys for better fracture toughness. However, invoking the described model to predict the behavior of underaged alloys which would have much finer precipitate diameters leads to the conclusion that the underaged alloys would have much lower toughness values than all of these alloys (since Eq. [1] would be much larger due to the $1/d$ dependence and predicts even coarser slip). Examination of Figure 20 helps understand this dilemma. Albrecht and Lutjering[47] examined the slip behavior of an underaged Al-Zn-Mg alloy that was deformed two pct, and have demonstrated that the grain boundaries have actually deformed

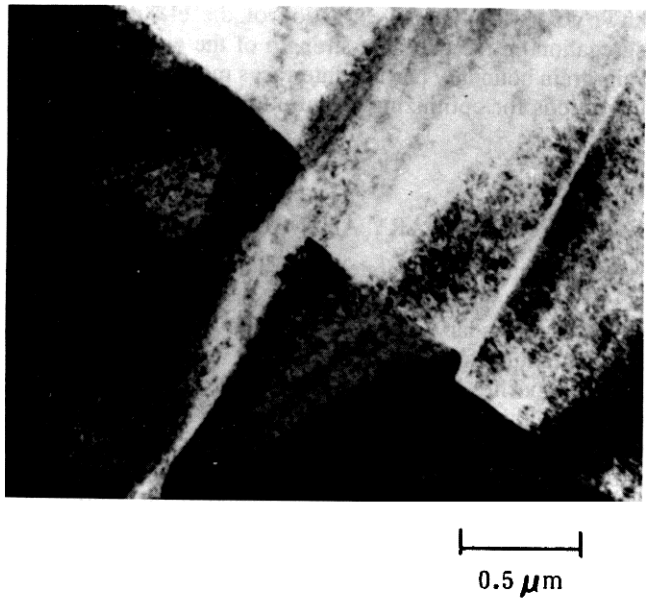

Fig. 20—Coarse slip bands in an underaged Al-Zn-Mg alloy (from Reference 47).

severely without void initiation. The grain boundaries have a ratcheted appearance, since they picked up "jogs" where intense slip bands intersected them. Note that no PFZ is evident. Similar observations of deformation behavior have been made in Al-Li alloys by Sanders, *et al.*[48] In the T6 temper, however, there exists a PFZ. When a slip band intersects a grain boundary, the strain localization must be accommodated. Due to the copious precipitation that has been induced by the T6 aging treatment, the grains on either side of their common boundary have been significantly strengthened. Hence, they can offer constraint against any deformation. However, the PFZ exists along the boundary. As was shown in Figure 18b, the strain localization at the slip band – grain boundary intersections can be accommodated by deformation within the PFZ and finally by void initiation, since the adjacent grain offers constraint against jog formation. The inability of the adjacent grain to deform homogeneously would further contribute to its lack of ability to accommodate any strain localization. Therefore, this indicates that the strain differential between the grain matrix and the precipitate free zone (σ_M-σ_{PFZ}), provides a relative measure of the tendency of these alloys to have intergranular void formation. Similarly, in considering grain boundary shear as a mechanism for void formation, this factor would indicate the tendency toward shear concentration within the grain boundary PFZ region. For either mechanism, the smaller (σ_M-σ_{PFZ}) is, the more favorable the overall deformation behavior would be, *i.e.*, strain would be more equally dissipated by the grain matrices and precipitate free zones. Welpmann, *et al*,[49] have suggested that the macroscopic ductility is determined mainly by this factor and the grain boundary length, since they felt that these two factors controlled the amount of grain boundary shear that would occur before final fracture.

The factor (σ_M-σ_{PFZ}) increases with increased solute content for the alloys in this study in the T6 temper. This is based on the assumption that the PFZ strength is comparable to that of the alloy as solution treated and that this strength is approximately the same for all of the alloys. For any significant increase in strength due to solid solution strengthening, a high solubility of one element with an appreciable size difference from the base metal and a distortion of tetragonal symmetry is required.[50] This is not the case for the Al-Zn-Mg system, so therefore the assumption of comparable solution treated strengths and therefore comparable PFZ strengths is not a bad one.

Therefore, for the alloys in this study, the fracture toughness has been shown to decrease as the tendency for both coarse slip and the term (σ_M-σ_{PFZ}) increases. (σ_M-σ_{PFZ}) is a relative measure of competition between matrix and PFZ deformation and therefore of a tendency toward intergranular fracture. These two factors can be used to qualitatively explain the fracture toughness behavior of Al-Zn-Mg alloys as a function of aging time and temperature. This is possible because the aging time and temperature affect the precipitate morphology and dispersion, which, in turn, control the subsequent matrix slip behavior and matrix strength.

C. *Influence of Plane Stress vs Plane Strain Conditions on Fracture Behavior*

Voids have been seen to nucleate at some of the grain boundary dispersoids in the *low solute* alloy at the higher strain level. However, no significant amount of intergranular fracture was observed in the final fracture. This alloy has the least coarse slip behavior and the smallest (σ_M-σ_{PFZ}) term and therefore would be expected to have better toughness and less intergranular fracture. As mentioned earlier, in order for the intergranular fracture to open parallel to the loading axis, the assistance of a σ_3 (through the thickness) stress is necessary. Hahn and Rosenfield[51] have demonstrated on 4340 steel that in order to obtain a plane stress fracture, the plastic zone size should be greater than four times the specimen thickness ($4t$). Table X lists the plastic zone sizes for these alloys in comparison with $4t$. Note that a minimum of at least 15 grain diameters are encompassed by the plastic zones of these alloys. This reinforces the theme that the overall grain deformation behavior and not just that of the PFZ is important. Only the *low solute* alloy satisfies this requirement ($r_p > 4t$) for a total plane stress fracture. Plane strain conditions will exist over part of the crack front for the higher solute alloys. When a state of plane stress exists, due to a large plastic zone, the specimen cannot support a σ_3 load through the sheet thickness. Therefore, for the *low solute* alloy, there will be no σ_3 available to open (assist void growth and coalescence) the grain boundaries parallel to the loading direction. A slanted shear fracture along macroscopic maximum shear planes would be expected and, indeed, is observed.

Table X. Calculated Plastic Zone Sizes

Alloy	Plastic Zone Size,* r_p (mm)	4 × Thickness, $4t$ (mm)
Low solute	6.9	6.4
Intermediate solute	1.3	6.4
High solute A	0.6	6.4
High solute B	0.7	6.4

*$r_p \simeq \frac{1}{2\pi}\left(\frac{K_c}{\sigma_{ys}}\right)^2$

The above argument suggests that if the higher solute alloys were available in thinner gauge sheet such that the relationship $r_p > 4t$ were valid, a slant fracture would result. A predominantly transgranular fracture mode would result if the σ_3 stress were solely responsible for assisting the intergranular separation once voids were initiated at slip band – grain boundary intersections. However, coarser matrix slip and a larger $(\sigma_M - \sigma_{PFZ})$ value would still exist, and hence they may override this stress effect. This discussion reinforces the necessity of evaluating material behavior from a mechanistic as well as from a microstructure approach. For example, a stronger material will be thinner if it replaces a weaker one and, therefore, should be evaluated at the thinner gage.

D. *Optimization of Fracture Toughness*

From the results of this research several suggestions can be made to optimize fracture toughness of ultrahigh strength 7XXX series aluminum alloys. The most obvious one is to develop more homogeneous matrix slip for the maximum strength condition. This may be accomplished by controlling ingot homogenization and processing procedures to develop a finer dispersoid population which would still be large enough $(d > d_c)$ to induce Orowan bowing. Since the dispersoids would be smaller, fracture initiation would also be delayed. In addition, if the dispersoids were coherent (*e.g.*, Zr-dispersoids, Zr_3Al), the problem of fracture initiation by matrix-dispersoid interface decohesion would be lessened. Another technique that has been used involves a thermal mechanical processing (TMP) sequence[52] to induce homogeneous deformation by deforming the alloy in the maximum strength condition at a temperature at or just above the G.P. solvus temperature.

Varying the slip behavior, however, is not sufficient in itself to obtain the maximum fracture toughness. Grain boundary shear will dominate and initiate the intergranular dimpled rupture fracture when the matrix slip is homogeneous and the term $(\sigma_M - \sigma_{PFZ})$ is large. Reducing the effective grain boundary length (or grain size) will decrease the amount of grain boundary shear that must be accommodated by triple points and grain boundary particles for a given macroscopic strain. Void initiation will be delayed and toughness enhanced. Therefore, inducing jogs on the grain boundaries *via* some TMP step or decreasing the grain size will be beneficial. On the other hand, if the PFZ could be eliminated entirely, the problem of grain boundary shear would be drastically reduced. Ag[53] additions have been shown to be beneficial in eliminating the PFZ. The determination of a less expensive alloying addition with the same result would be significant.

An ultrasonic preaging treatment being pursued by Shea and Rao[54] may eliminate the PFZ entirely, or at least significantly increase its strength. This technique has been shown to develop a dislocation network in the vicinity of grain boundaries for a 304 stainless steel alloy, while having little effect on the grain interior substructure. If this network can promote sufficient heterogeneous nucleation in the grain boundary region during subsequent aging treatments, the influence of the factor $(\sigma_M - \sigma_{PFZ})$ may be substantially diminished, and higher fracture toughness would result.

Solute segregation to the grain boundaries has been shown to exist.[49] An investigation of the effect of solute segregation on the cohesive strength of the grain-grain and grain-grain boundary particle interfaces may provide further suggestions for optimizing fracture toughness.

VI. SUMMARY AND CONCLUSIONS

Previous studies and models have attempted to explain the loss of fracture toughness in 7XXX series aluminum alloys with grain boundary shear mechanisms and on the amount of intergranular fracture. For the sheet alloys in this study, these approaches have been proved inadequate. The difference in toughness between the *intermediate* and *high solute* alloys (both have the same amount of intergranular fracture) can be explained only *via* the mechanism proposed in this study, since differences in matrix behavior are shown to affect fracture initiation. Some intergranular fracture due to grain boundary shear, as well as an occasional transgranular shear fracture, were observed in the higher solute alloys.

Fracture initiation has been shown to occur at the Cr-dispersoids for both the transgranular and intergranular fractures. Evidence existed previously that correlated the fine transgranular dimples observed in 7XXX series alloys with these dispersoids. However, this research disproves a previously accepted suggestion that all intergranular fracture in these alloys initiates at the grain boundary η-precipitate. It has been unequivocally demonstrated that for the T6 temper intergranular fracture initiates at grain boundary Cr-dispersoids. The η precipitates facilitate void coalescence and final fracture. This occurs as voids associated with the Cr-dispersoids grow and voids nucleate at the η at higher strain levels. This has been clearly shown. Only in grossly overaged alloys where the average grain boundary η precipitate size would be equal to or larger than the Cr-dispersoids would they be expected to initiate intergranular fracture first.

This research has proposed that the fracture toughness behavior of these alloys is dependent on two parameters. These are the coarseness of matrix slip and the difference in strength between the matrix and PFZ, $(\sigma_M - \sigma_{PFZ})$. The higher solute alloys had coarser slip than the *low solute* alloy and larger $(\sigma_M - \sigma_{PFZ})$ values. A model by Hornbogen and Gahr predicts the difference in coarseness of slip of three alloys. The term $(\sigma_M - \sigma_{PFZ})$ can be considered a relative measure of the tendency toward intergranular fracture. This is because the higher $(\sigma_M - \sigma_{PFZ})$ is, the more likely void initiation will occur within the PFZ. For large $(\sigma_M - \sigma_{PFZ})$ values, intergranular fracture *via* slip band – grain boundary void initiation dominates when matrix slip is inhomogeneous. For homogeneous matrix slip, intergranular fracture would be controlled by the grain boundary shearing mechanism.

The coarseness of slip and $(\sigma_M - \sigma_{PFZ})$ factors can not only be used to rank the fracture toughness as a function of yield strength, but they enable a qualitative explanation for the shape of the toughness *vs* yield strength curve as a function of both aging time and temperature. These two parameters can also be used to explain the effects of grain size, precipitate morphology, areal fraction of grain boundary precipitate, and thermal-mechanical processing (TMP) on fracture toughness.

ACKNOWLEDGMENTS

The authors express their sincere appreciation to Dr. J. R. Low, Jr., who initiated this research program and provided valuable guidance until his retirement in August 1977. The authors also wish to thank Dr. H. Y. Hunsicker and Mr. J. T. Staley of the Alcoa Technical Center for their assistance. Under their direction, the difficult task of producing ultrahigh purity alloys was successfully accomplished. In addition, the sponsorship and financial assistance of the National Science Foundation at Washington, DC under NSF Grant DMR76-02244 is acknowledged and duly appreciated, as is support from the Materials Research Laboratory Section of NSF through the use of central facilities.

REFERENCES

1. J. A. Nock and N. Y. Hunsicker: *J. Metals*, 1963, vol. 15, no. 3, p. 216.
2. D. S. Thompson and R. E. Zinkham: *Eng. Fract. Mech.*, 1975, vol. 7, p. 389.
3. G. T. Hahn and A. R. Rosenfield: *Metall. Trans. A*, 1975, vol. 6A, p. 653.
4. M. Graf and E. Hornbogen: *Acta Met.*, 1977, vol. 25, p. 883.
5. A. H. Geisler: *Phase Transformation in Solids*, R. Smoluckowski, J. E. Mayer, and W. A. Weyl, eds., Wiley, New York, NY, 1951, p. 387.
6. J. L. Taylor: *J. Inst. Met.*, 1963/64, vol. 92, p. 301.
7. N. Ryum: *Acta Met.*, 1968, vol. 16, p. 327.
8. S. Kirman: *Metall. Trans.*, 1971, vol. 2, p. 1761.
9. P. N. T. Unwin and G. C. Smith: *J. Inst. Met.*, 1969, vol. 97, p. 299.
10. R. H. Van Stone, R. H. Merchant, and J. R. Low, Jr.: *ASTM STP* 556, 1974, p. 93.
11. D. Broek: *Eng. Fract. Mech.*, 1973, vol. 5, p. 55.
12. J. T. Staley: Alcoa Technical Center, Alcoa Center, PA, unpublished research, 1974.
13. B. J. Dunwoody, D. M. Moore, and A. T. Thomas: *J. Inst. Met.*, 1973, vol. 101, p. 172.
14. J. M. Dowling and J. W. Martin: *Proceedings of the Third International Conference on the Strength of Metals and Alloys*, Institute of Metals and The Iron and Steel Institute, London, 1973, p. 170.
15. G. Lutjering and A. H. Gysler: *Verformungsmechanismen und Struktur in der plastischen Zone vor Risspitzen*, Seminarbericht 20 kV – Hochspannungselektronenmikroskopie, Munich, 1974, p. 9.
16. G. Lutjering: Ruhr-Universitat Bochum, Institut fur Werkstoffe, Bochum, Germany, unpublished research, 1976.
17. T. Mori and T. Mura: *Mat. Sci. Eng.*, 1976, vol. 26, p. 89.
18. D. Broek: *NLR TR 72 029-u*, National Aerospace Labs, The Netherlands, 1972.
19. R. H. Van Stone and J. A. Psioda: *Metall. Trans. A*, 1975, vol. 6A, p. 668.
20. J. S. Santer: *Metall. Trans. A*, 1978, vol. 9A, p. 769.
21. T. M. F. Ronald and D. P. Voss: Metals and Ceramics Synthesis Branch, Wright Patterson Air Force Base, OH, unpublished research.
22. J. C. W. Van der Kastelle and D. Broek: *Eng. Fract. Mech.*, 1977, vol. 9, p. 625.
23. G. M. Ludtka and D. E. Laughlin: *Metall. Trans. A*, 1981, vol. 12A, p. 2083.
24. ASTM E8-69, *Annual Book of ASTM Standards*, 1969, vol. 31, p. 196.
25. N. A. Kahn and E. A. Imbenbo: *The Welding Journal*, 1958, vol. 27, p. 169-s.
26. J. G. Kaufman and J. F. Reedy: "Description and Procedure for Making Kahn-Type Tear Tests," Alcoa Laboratories Report, no. 9-M-681, Alcoa Technical Center, Alcoa Center, PA, February 10, 1966.
27. J. G. Kaufman and M. Holt: *Advances in Cryogenic Engineering*, 1965, vol. 10, p. 216.
28. J. G. Kaufman and A. H. Knoll: *Mat. Res. and Standards*, 1964, vol. 4, p. 151.
29. J. G. Kaufman and E. W. Johnson: *ASTM Proceedings*, 1963, vol. 62, p. 778.
30. R. H. Heyer: *ASTM STP* 381, 1965, p. 113.
31. J. G. Kaufman and E. W. Johnson: *Advances in Cryogenic Engineering*, 1963, vol. 8, p. 678.
32. M. P. Hanson, G. W. Stickley, and H. T. Richards: *ASTM STP* 287, 1960, p. 3.
33. ASTM E561-76T, *Annual Book of ASTM Standards*, 1976, vol. 31, p. 539.
34. G. M. Ludtka: Ph.D. Thesis, Carnegie-Mellon University, Pittsburgh, PA, 1978.
35. J. R. Rice: *J. Appl. Mech.*, 1968, vol. 35, p. 379.
36. J. A. Begley and J. D. Landes: *ASTM STP* 514, 1972, p.1.
37. K. G. Broberg: *J. Mech. Phys. Solids*, 1971, vol. 19, p. 407.
38. J. P. Hickerson, Jr.: *Eng. Fract. Mech.*, 1977, vol. 9, p. 76.
39. W. R. Warke, N. A. Neilson, R. W. Hertzberg, M. S. Hunter, and M. Hill: *ASTM STP* 436, 1968, p. 212.
40. R. H. Van Stone and T. B. Cox: *ASTM STP* 600, 1976, p. 5.
41. R. J. Price and A. Kelly: *Acta Met.*, 1964, vol. 12, p. 979.
42. G. I. Taylor: *J. Inst. Met.*, 1938, vol. 62, p. 307.
43. A. Gysler, S. Lutjering, and V. Gerold: *Acta Met.*, 1974, vol. 22, p. 901.
44. G. Gutjering and S. Weissman: *Acta Met.*, 1970, vol. 18, p. 785.
45. J. D. Evensen, N. Ryum, and J. D. Embury: *Mat. Sci. Eng.*, 1975, vol. 18, p. 221.
46. E. Hornbogen and K. H. zum Gahr: *Metallography*, 1975, vol. 8, p. 181.
47. J. Albrecht and G. Lutjering: *Einfluss der Mikrostruktur auf die Ermudungsrissausbreitung in Aluminum–Legierungen*, Forschungsbericht der Deutchen Luft–und Raumfahrt, DLR-EB77-07, Cologne, 1977.
48. T. H. Sanders, Jr., E. A. Ludwiczak, and R. R. Sawtell: *Mat. Sci. Eng.*, 1980, vol. 43, p. 247.
49. K. Welpmann, G. Lutjering, and W. Bunk: *Fracture 1977*, 2, ICF4, Waterloo, Canada, June 19-24, 1977.
50. R. B. Nicholson: "Strong Microstructures from the Solid State," in *Strengthening Methods in Crystals*, A. Kelly and R. B. Nicholson, eds., Halsted Press, New York, NY, 1971, p. 553.
51. G. T. Hahn and A. R. Rosenfield: *ASTM STP* 432, 1968, p. 5.
52. N. E. Paton and A. W. Sommer: *Proceedings of the Third International Conference on the Strength of Metals and Alloys*, Institute of Metals and The Iron and Steel Institute, London, 1973, p. 106.
53. I. J. Polmear: *J. Inst. Met.*, 1960, vol. 89, p. 51.
54. M. M. Shea and B. V. N. Rao: "Influence of Ultrasonic Treatment on the Substructure in 304 Stainless Steel," GM Research Publication GMR-3404, September 1980.